Anharmonic lattice dynamics and the origin of intrinsic ultralow thermal conductivity in AgI materials

Yan Wang, Quan Gan, Mingyuan Hu, Jinhong Li, Lin Xie [*], and Jiaqing He[†]

Department of Physics, Southern University of Science and Technology, Shenzhen, 518055, China

Ionic conductors such as AgI with ultralow thermal conductivities (κ_l) are of increasing interest because of their excellent thermoelectric properties. However, the origin of their intrinsic low κ_l values remain elusive. In this study, comprehensive theoretical calculations of the lattice dynamics and the thermal transport properties of γ-AgI (zinc-blende structure) and β-AgI (wurtzite structure) as functions of temperature were carried out based on many-body perturbation theory and phonon Boltzmann transport theory. First, the mean-squared displacements (MSDs) of Ag^+ were significantly larger than those of I^- in both γ- and β-phases below the order-disorder phase transition temperature (T_c), which led to a characteristic "rattling" feature and low-frequency, nearly flat local phonon vibrations. According to our previous work [Xie *et al.*, Phys. Rev. Lett. **125**, 245901 (2020)], such nondispersive flat phonon band structures are expected to give rise to four-phonon resonance and result in a dramatic increase in the four-phonon scattering over the conventional three-phonon scattering. For γ-AgI, similar four-phonon resonance behavior was also discovered for the low-lying transverse acoustic phonon branches, and it was found that their four-phonon scattering rates were an order of magnitude larger than the corresponding three-phonon scattering rates. Considering the four-phonon scattering, the theoretical κ_l of γ-AgI was predicted to be ~ 0.32 W/m K at 300 K, which was in good agreement with the value deduced from our experiments (~ 0.36 W/m K at 300 K). Compared to γ-AgI, the acoustic phonons in β-AgI were more dispersive, and they intertwined with low-energy optical phonons at the zone boundaries. It was found that three-phonon resonance became as important as four-phonon resonance for the nearly flat longitudinal phonon band. The theoretical κ_l for β-AgI was determined to be around ~ 0.32 W/m K at room temperature, closely reproducing our measurement value ~ 0.29 W/m K. Our results for AgI demonstrate the strong quartic anharmonicity in materials characterized by the rattling of weak bonding atoms as well as dispersionless phonon band structures. It is believed that this intimate relationship between the low-κ_l and flat phonon dispersion can be employed as a good indicator when searching for material systems with ultralow κ_l values, e.g., cagelike rattling structures, quasi-two-dimensional structures, and chainlike structures.

I. INTRODUCTION

Materials with ultralow lattice thermal conductivities have attracted great attention because of their potential uses in practical applications, e.g., thermoelectric (TE) devices. The use of nanocrystallization and the introduction of hierarchical structures has proven to be an effective strategy for lowering κ_l, which is closely related to the increased phonon scattering and decreased group velocity caused by grain boundaries and defects [1–4]. In addition to optimizing the κ_l values of existing materials to improve energy-conversion efficiency, a search for new materials is also inevitable in order to obtain outstanding TE properties. The key to finding new materials lies in anharmonic interactions, which trigger additional phonon-phonon scattering and result in low lattice thermal conductivities. One of the most common and simplest methods is to introduce "rattling" [5,6]. For example, materials like clathrates and skutterudites are a certain class of new TE

materials with exceptionally low κ_l values [7–10]. They typically have complex, periodic, cagelike crystal structures with a specific guest atom rattling in the center. The weak bonding between the guest- and the neighboring host atoms leads to large vibration amplitudes of the guest atom. In addition to the materials with such apparent cagelike, complex structures, Li *et al.* proposed that rattling can also be introduced into materials with simple structures as long as the vibrations of an atom are substantially larger than those of its neighboring atoms [8]. For example, single-crystalline Tl_3VSe_4, with a simple body-centered-cubic lattice structure, has been recently reported to have an ultralow $\kappa_l \approx 0.3$ W/m K at 300 K [11], in which the Tl atoms have larger mean-squared displacements (MSDs) than their surrounding atoms. Thus, ultralow κ_l materials can be sought from the materials that exhibit the rattling mode, in which there are large MSD discrepancies between atoms. For instance, the typical ionic conductors are good candidates, e.g., $Cu_{2-x}Se$ and $AgCrSe_2$ due to the larger vibration amplitudes of mobile Cu^+ or Ag^+ ions than their surrounding anions [12–15].

In principle, guest atoms vibrating with larger atomic displacements in comparison to the neighboring atoms lead

---

[*]xiel3@sustech.edu.cn
[†]hejq@sustech.edu.cn

to significant anharmonicity, which thus lowers κ_l. Based on the first-principles calculation, the anharmonicity and thermal transport can be explained in the framework of the many-body perturbation theory. The lowest-order perturbation theory, i.e., three-phonon interactions, has been shown to work well for relatively simple materials with stiff bonds and high three-phonon scattering phase spaces, and the results are in good agreement with experiments [16–20]. However, it has recently been found that three-phonon interactions fail to describe materials with weak interatomic bonding or small three-phonon scattering spaces. In this case, higher-order perturbation theory and four-phonon scattering processes have attracted attention for their improved description of the thermal transport physics in those materials, e.g., BAs, TaN, α-Al$_2$O$_3$, and AlSb [13,21–24]. According to Feng *et al.*, three-phonon processes are described by the first-order perturbation $H'_{\lambda_1\lambda_2\lambda_3}$, which include splitting processes ($\lambda_1 \rightarrow \lambda_2 + \lambda_3$) and combination processes ($\lambda_1 + \lambda_2 \rightarrow \lambda_3$) [21]. The four-phonon scattering processes are described by the second perturbation term $H''_{\lambda_1\lambda_2\lambda_3\lambda_4}$, which include three kinds of processes: traditional splitting, combined processes ($\lambda_1 \rightarrow \lambda_2 + \lambda_3 + \lambda_4$, $\lambda_1 + \lambda_2 + \lambda_3 \rightarrow \lambda_4$), and the redistribution process ($\lambda_1 + \lambda_2 \rightarrow \lambda_3 + \lambda_4$) [25]. To further illustrate these phonon-scattering processes, we have drawn a schematic of the phonon-phonon scattering processes in Fig. S1(Supplemental Material) [26]. Although considering high-order perturbation terms is a more rigorous approach for determining the heat-transport properties, it is still almost impractical to perform large-scale high-throughput screening due to the high computing cost. To avoid the waste of computing resources, we reviewed and summarized some particular characteristics of the reported dominant four-phonon scattering materials. There are two types of remarkable features in phonon dispersion for materials exhibiting strong four-phonon scattering effects: (1) large phonon band gaps [27] and phonon energy bunching [28], which suppress the phase space for the three-phonon scattering while allowing four-phonon processes; and (2) flat phonon dispersions [25] that favor four-phonon redistribution processes. Materials with the above-mentioned characteristics usually have strong anharmonicity, and four-phonon scattering or even higher-order scattering processes are in principle non-negligible.

AgI as an ionic conductor in solid electrolytes has attracted great attention. Above $T_c \sim 420$ K, it is a superionic conductor with the body-centered-cubic $Im\bar{3}m$ structure (α phase) [29–31]. In the superionic conducting phase, some of the Ag$^+$ cations are disordered across the tetrahedral interstices formed by I [32]. Below T_c, it is suggested that AgI is stable with the coexistence of a zinc-blende γ phase (space group: $F\bar{4}3m$) and wurtzite β phase (space group: $P\bar{6}_3mc$) [33–37]. The atomic structures of γ- and β-AgI are displayed in Fig. 1, in which γ-AgI has iodine anions in a cubic-close-packed structure. Meanwhile, β-AgI consists of stacked iodine tetrahedra with a silver atom in the center [35,37,38]. Both yield a four-coordinated lattice, in which each atom is surrounded by four heterogeneous atoms as its nearest neighbors. Experiments showed that the κ_l value of β-AgI is extremely low (~ 0.36 W/m K at 300 K) [39], but the measurement of γ-AgI is still lacking. In comparison, the theoretical κ_l values β-phase AgI at 300 K in the literature were reported
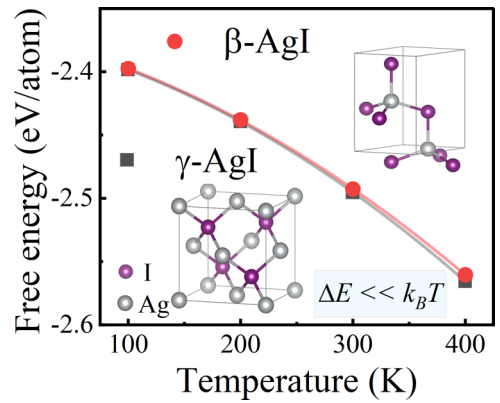

FIG. 1. Helmholtz free energies of γ- and β-AgI, with the wurtzite and zinc-blende structures drawn in the insets.

to be around 1.5 W/m K [40], which are more than five times higher than the experimental values. The results indicate that the lowest-order three-phonon interactions cannot fully describe the anharmonicity and heat transport of AgI. In this work, we found that the phonon dispersions of γ- and β-phase AgI exhibit the characteristic four-phonon scattering features mentioned above and show that the four-phonon scattering processes lead to the intrinsic ultralow lattice thermal conductivity of AgI. To further verify the importance of fourth-order perturbation in AgI, the thermal conductivity of single-phase crystal β-phase AgI is measured in our work. The thermal conductivity of single-phase crystal γ-phase AgI is deduced from our measurement values of β-AgI and two-phase mixture. Our theoretical predicted κ_l of both γ- and β-AgI are comparable with experiments. Combining theory and experiment, the significant effects of four-phonon scattering process on thermal transport in AgI are verified.

II. MATERIALS AND METHODS

A. Calculation details

In this work, the calculations of the anharmonic lattice dynamics of AgI were carried out using the temperature-dependent effective potential method (TDEP) and the *ab initio* molecular dynamics (AIMD) implemented via the VASP code [41,42]. A supercell with a total number of 250 atoms for the zinc-blende cubic γ-phase AgI and a supercell with 228 atoms for the hexagonal β-phase AgI were used throughout the molecular dynamics (MD) simulations. The AIMD simulation was performed with a plane-wave cutoff of 550 eV, Γ-point sampling, and a time step of 2 fs in the *NVT* ensemble. In order to ensure the external pressure was around ambient pressure, several short AIMD simulations with different initial configurations at 300 K (total time steps = 1000 steps) were carried out first. Then, the most stable configuration was further used to run a 3000-time-step AIMD simulation. From these 3000 MD configurations, 20 configurations were chosen stochastically based on the last 1000 steps. Then, a new 1000-time-step AIMD simulation for each new configuration was performed again, and 20 000 configurations were obtained in total. Using this method, we voided the high cost of long AIMD runtimes while guaranteeing precision

at the same time [43]. After, 200 representative uncorrelated configurations were chosen by Monte Carlo sampling, and self-consistent calculation was performed again for those 200 configurations with a finer $2 \times 2 \times 2$ Monkhorst-Pack mesh and a convergence threshold of the total energy of 10^{-6} eV. The as-obtained potential energy U including anharmonic terms is as follows:

$$U = U_0 + \sum_i \frac{P_i^2}{2m_i} + \frac{1}{2!} \sum_{ij} \sum_{\alpha\beta} \Phi_{ij}^{\alpha\beta} u_i^\alpha u_j^\beta$$

$$+ \frac{1}{3!} \sum_{ijk} \sum_{\alpha\beta\gamma} \Phi_{ijk}^{\alpha\beta\gamma} u_i^\alpha u_j^\beta u_k^\gamma$$

$$+ \frac{1}{4!} \sum_{ijkl} \sum_{\alpha\beta\gamma\delta} \Phi_{ijkl}^{\alpha\beta\gamma\delta} u_i^\alpha u_j^\beta u_k^\gamma u_l^\delta + \dots, \tag{1}$$

where u_i denotes the displacement of atom i, α, β, γ, and δ are Cartesian indices, and Φ is the $n\text{th} - \text{order}$ interatomic force constants (IFCs), which is equal to the derivative of the potential energy. Then, the temperature-dependent force constants, including the long-range dipole-dipole interactions, were obtained using the TDEP software package [44,45]. The cutoffs for the second, third, and fourth IFCs were 9.0, 7.0, and 4.6 Å for the γ phase, and 9.0, 7.0, and 5.0 Å for the β phase, respectively. Theoretical calculations of the lattice thermal conductivity were based on the phonon Boltzmann transport equation [17,21,46,47], which is

$$\kappa = \frac{1}{V} \sum_\lambda \upsilon_\lambda^2 C_\lambda \tau_\lambda, \tag{2}$$

where λ specifies the phonon mode; V is the volume of the unit cell; and υ_λ, C_λ, and τ_λ are the group velocity, specific heat, and phonon relaxation time, respectively. The scattering rate can be written as the inverse of the phonon relaxation time, τ^{-1}. To solve Eq. (2), we obtain τ_λ from many-body perturbation theory. The total Hamiltonian H including four-phonon interactions can be expressed as [21,48]

$$H = H_0 + H' + H'' + \dots \tag{3}$$

$$H_0 = \sum_\lambda \hbar\omega_\lambda \left(a_\lambda^\dagger a_\lambda + \frac{1}{2} \right) \tag{4}$$

$$H' = \sum_{\lambda_1\lambda_2\lambda_3} H'_{\lambda_1\lambda_2\lambda_3} \left(a_{-\lambda_1}^\dagger + a_{\lambda_1} \right)\left(a_{-\lambda_2}^\dagger + a_{\lambda_2} \right)\left(a_{-\lambda_3}^\dagger + a_{\lambda_3} \right) \tag{5}$$

$$H'' = \sum_{\lambda_1\lambda_2\lambda_3\lambda_4} H''_{\lambda_1\lambda_2\lambda_3\lambda_4} \left(a_{-\lambda_1}^\dagger + a_{\lambda_1} \right)\left(a_{-\lambda_2}^\dagger + a_{\lambda_2} \right)\left(a_{-\lambda_3}^\dagger + a_{\lambda_3} \right)$$
$$\times \left(a_{-\lambda_4}^\dagger + a_{\lambda_4} \right), \tag{6}$$

where H_0 is the harmonic term, and H' and H'' are the three-phonon and four-phonon perturbations, respectively. $a_\lambda^\dagger$ and a_λ in Eqs. (4)–(6) denote the creation and annihilation operators, and ω_λ is the angular frequency of the phonon mode λ. With the second-order perturbation term, the current computing resources are limited when fully solving the

Boltzmann phonon-transport equation. Therefore, we consider the phonon-scattering process with the simple relaxation time approximation as follows:

$$\tau^{-1} = \tau_{3ph}^{-1} + \tau_{4ph}^{-1}, \tag{7}$$

where τ_{3ph}^{-1} and τ_{4ph}^{-1} represent the phonon-scattering rates due to three- and four-phonon interactions, respectively. The scattering rate can be rewritten as

$$\tau^{-1} = 2\Gamma' + 2\Gamma'', \tag{8}$$

where $2\Gamma'$ and $2\Gamma''$ represent the linewidths equal to the imaginary part of the phonon self-energy due to three-phonon and four-phonon scattering processes, respectively. The spectral function and self-energy for the lowest-order perturbation were calculated with a Monkhorst-Pack mesh grid with dimensions of $35 \times 35 \times 35$ for the γ phase and $38 \times 38 \times 19$ for the β phase. Due to the high computing cost, $10 \times 10 \times 10$ and $10 \times 10 \times 5$ Monkhorst-Pack mesh grids were used for the γ- and β-phase AgI when four-phonon interaction processes were considered.

B. Experimental details

We grew a β-phase AgI crystal using a temperature gradient method. We first transferred the starting mixed-phase, AgI (Aladdin, 99.99%) powder into a quartz tube. Then, the tube was evacuated to a pressure of $\sim 10^{-3}$ Pa and flame sealed. The tube was inserted into a larger fused-silica tube to avoid breaking the tube due to the phase transitions and the considerable differences in the thermal expansion between the crystal and silica. After the above processes, the tubes were evacuated and flame sealed again to avoid crystal formation from oxidation by the air. The tube was slowly heated to 1023 K in 6 h and maintained at this temperature for 12 h to completely melt the AgI powder. To maintain a temperature difference of 130 K between the upper and lower parts of the tube, the high-temperature region and low-temperature region were cooled slowly to 803 and 673 K, respectively. This temperature was maintained for 24 h to ensure the crystal was solidified. Finally, the high-temperature and low-temperature regions were cooled to 423 K simultaneously and kept at this temperature for 120 h. To obtain a dense bulk mixture of AgI, the powder was cold pressed into a cylinder with a diameter of 10 mm and height of 8 mm. After, the cylinder was inserted in a cubic press (DS 6×10 MN) under a pressure of 1 GPa and held at this pressure for 5 min.

X-ray diffraction (XRD) was performed with a Rigaku SmartLab 9-KW diffractometer operating with Cu Kα1 x-ray radiation ($\lambda = 1.5406$ Å). The Rietveld refinement analyses of the XRD results of AgI (Aladdin, 99.99%) powder showed that the γ- and β-phase AgI coexisted at room temperature with a mass ratio of 47:53 [49,50]. Variable-temperature XRD experiments were carried out every 20 K between 300 and 400 K for our prepared single β-phase polycrystalline sample. The variable-temperature XRD data confirmed that there was no phase transition between the β- and γ-phase AgI in the range of 300–400 K, which indicated that our single-phase sample was stable under 400 K.

Measurement of the lattice thermal conductivities of the polycrystalline β-phase AgI and multiphase mixture AgI were

performed on $3 \times 3 \times 2-\text{mm}^3$ samples using the Thermal Transport Option for Physical Property Measurement System [51]. A two-point measurement geometry was used with heat flow along the 2-mm dimension to reduce the heat-radiation losses during the measurement.

III. RESULTS AND DISCUSSION

A. Phase stability

It is well known that the stable wurtzite AgI structure and the metastable zinc-blende AgI structure coexist at room temperature [29,37,39,52]. There are some overall similarities between these allotrope structures. For example, both yield a four-coordinated lattice, in which each atom is surrounded by four heterogeneous atoms as nearest neighbors [38]. Thus, the γ- and β-phase AgI have almost the same heat capacities, phase transition temperatures, and enthalpies of phase transition [33,53]. It is difficult to separate the two mixed phases, and there are also some disagreements about the phase stability. Some researchers suggest that the γ-phase is metastable at all temperature ranges [30,33], while only the β-phase is thermodynamically stable at ambient atmospheric conditions. However, it was found experimentally that the β- and γ-polymorphs form in the same ratio when samples are cooled after heating just based on the transition temperature [31,32,35]. Due to the controversy over phase stability, comprehensive research on AgI at room temperature is still lacking. Here, we studied the phase stability of both β- and γ-AgI in terms of their thermodynamics and lattice dynamics.

The theoretical phase stability can be investigated by minimizing the Helmholtz free energy, $F = U - TS$, where U is potential energy, T is temperature, and S is entropy. In the harmonic approximation, the integral form of the free energy F is obtained from

$$F_{\text{vib}} = \int_0^\infty g(\omega)\left\{ k_B T \ln\left[1 - e^{-(\hbar\omega/k_B T)}\right] + \frac{\hbar\omega}{2} \right\} d\omega, \quad (9)$$

where $g(\omega)$ is the phonon density of states, k_B is the Boltzmann constant, and T is the temperature. Generally, the temperature effect is neglected and the potential energy of a static lattice is used [54]. Here, we take advantage of the method proposed by Hellman *et al.* to consider the third-order and fourth-order anharmonic corrections on potential energy as a function of temperature [55]. The temperature-dependent free energy can be calculated as

$$F_T = U_0 + F_{\text{vib}}, \quad (10)$$

$$U_0 = U_{\text{AIMD}}(t) - \frac{1}{2}\sum_{ij\alpha\beta} \Phi_{ij}^{\alpha\beta} u_i^\alpha(t) u_j^\beta(t)$$
$$- \frac{1}{6}\sum_{ijk\alpha\beta\gamma} \Phi_{ijk}^{\alpha\beta\gamma} u_i^\alpha(t) u_j^\beta(t) u_k^\gamma(t)$$
$$- \frac{1}{24}\sum_{ijkl\alpha\beta\gamma\delta} \Phi_{ijkl}^{\alpha\beta\gamma\delta} u_i^\alpha(t) u_j^\beta(t) u_k^\gamma(t) u_l^\delta(t), \quad (11)$$

where $U_{\text{AIMD}}(t)$ is the potential-energy surface calculated by AIMD; U_0 is the static lattice potential energy. Based on Eqs. (9)–(11), we studied the phase stability of the β- and
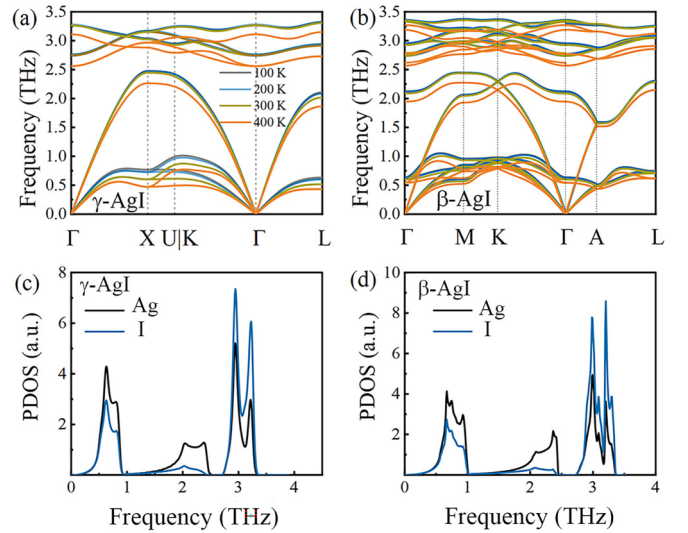

FIG. 2. Phonon dispersions of (a) γ-AgI and (b) β-AgI in the temperature range of 100–400 K. Atom-projected densities of states for (c) γ- and (d) β-phase AgI at 300 K.

γ-phases at different temperatures, and the results are shown in Fig. 1. The energy differences between these two phases are less than $k_B T$, e.g., the energy difference is ~ 0.003 eV, while $k_B T \sim 0.026$ eV at 300 K, which indicates that these two phases could coexist at room temperature. We also calculated the phonon dispersions of both the γ- and β-phases AgI in the temperature range of 100–400 K. As shown in Figs. 2(a) and 2(b), these two structures were dynamically stable, which further confirmed that both phases were stable from 100 to 400 K. As shown in Figs. 2(c) and 2(d), the partial phonon density of states (DOS) of Ag atoms dominated the low-frequency region with a sharper peak than that of I atoms, whereas I atoms contributed to the high-frequency DOS at 300 K (due to the negligible difference of the DOSs at different temperatures, only the results at room temperature are shown here). The stability and rattling thermal vibrations of AgI can be further validated by analyzing the MSD based on molecular dynamics and lattice dynamics. According to Ref. [45], the MSD of the jth atom can be expressed with harmonic approximation as

$$\langle |u^\alpha(jl,t)|^2 \rangle = \frac{\hbar}{2Nm_j} \sum_{q,\nu} \omega_\nu(q)^{-1} (1 + 2n_\nu(q,T)) |e_\nu^\alpha(j,q)|^2, \quad (12)$$

where t is the time, m_j is the mass of atom j, N is the number of the unit cells, q is the wave vector, ν is the index of the phonon mode, $n_\nu(q,T)$ is the phonon population, and the bracket $\langle |u^\alpha(jl,t)|^2 \rangle$ is the ensemble average over time in the lth unit cell. As shown by Eq. (12), the MSD of an atom is inversely proportional to its atomic mass. Thus, light atoms have the potential to give rise to larger MSDs. More importantly, the summation in Eq. (12) implies that MSD is also intimately related to the phonon frequency $\omega_\nu(q)$ weighted by the phonon population $n_\nu(q,T)$ and the atom-projected DOS $|e_\nu^\alpha(j,q)|^2$. Specifically, atoms with dense atom-projected DOSs [high $|e_\nu^\alpha(j,q)|^2$] and low phonon frequencies [large $\omega_\nu(q)^{-1}$] could result in larger MSDs as well.

TABLE I. Mean-squared displacements (Å^2) of γ- and β-phase AgI in the temperature range of 100–400 K from AIMD.

Atoms	100 K	200 K	300 K	400 K
		γ-phase AgI		
Ag	0.024	0.043	0.078	0.133
I	0.015	0.024	0.041	0.055
		β-phase AgI		
Ag	0.022	0.044	0.067	0.118
I	0.014	0.027	0.034	0.048

This was the reason that Ag atoms had larger MSDs (lower mass, higher projected DOSs at low frequencies). Harmonic approximation formulations above may be inadequate in describing AgI with remarkable anharmonicity, but are still useful to explain the appearance of significant MSDs difference between atoms. To include full anharmonic effects in the calculation, the long-time AIMD simulations of γ- and β-AgI at different temperatures are employed. Below T_c, no diffusion of Ag^+ and I^- ions was observed from our MD calculations, and the calculated MSDs are given in Table I. At room temperature, the calculated MSDs of Ag^+ in γ-phase AgI and β-phase AgI from the AIMD were ~ 0.078 and $\sim 0.067\,\text{Å}^2$, which were substantially larger than that of I^- (~ 0.041 and $\sim 0.034\,\text{Å}^2$), respectively. As a comparison, the experimental MSD values of Ag^+ and I^- were 0.074 and $0.043\,\text{Å}^2$, respectively [56,57]. All high-order anharmonic terms, thermal expansion, and renormalization of phonons are included within the molecular dynamics simulation [58,59], resulting in better agreements with the experiments than harmonic approximation (see the Supplemental Material). Similarly, an ionic conductor with dense low-frequency vibrations is more likely to have distinguishable MSDs between the cation and anion, e.g., AgBr, CuCl, CuI, and CuBr [57]. As we have discussed in the Introduction, the rattling mode applies when the vibration amplitudes between the guest atom and its neighboring atoms are distinguishable [8]. For example, Cu_3SbSe_3 [60], $CsCu_3O_2$ [8], $CsPbBr_3$ [61], Tl_3VSe_4 [11], and $TlInTe_2$ [62] are reported to have rattling-induced low thermal conductivities due to the larger MSDs of Cu, Cs, and Tl atoms. According to Table I, the MSD value of Ag^+ is much larger than that of I^-, which indicates that the guest atom Ag was rattling in its surrounding host I atoms and potentially led to strong anharmonicity.

B. Anharmonic phonon lattice dynamics

In this section, we focus on the anharmonic lattice dynamics of γ- and β-phase AgI in detail. As shown in Fig. 2(a), there was a large energy gap between the transverse acoustic (TA) phonons and the longitudinal acoustic (LA) or optical phonons in the γ-phase AgI. In the temperature range of 100–300 K, the optical branches and the LA phonon branch changed slightly. In contrast, the TA branches shifted down to a substantially lower-frequency region at 300 K, which resulted in a larger TA-LA and TA-O energy gap. Such a large phonon band gap is well known to forbid two TA phonons from combining into a new phonon, and only a high-order four-phonon scattering process is allowed. At a temperature

close to T_c (400 K), it was found that all the phonon branches softened, which was a clear indication of structural phase transitions. In addition, the closed acoustic branches bunched in the frequency range of 0–1 THz, which forbade three-phonon scattering processes. The split TA1 and TA2 branches parallel to each other along the path $X \rightarrow U|K \rightarrow \Gamma$ with flat phonon dispersion facilitated four-phonon recombination processes.

For β-phase AgI, two transverse optical phonons (denoted as TO1 and TO2) were intertwined with acoustic phonons at the zone boundaries below 1.0 THz. Because of the energy-conservation rule, the phase space of the three-phonon scattering that only involved a low-frequency channel was restricted [28,63]. The phonon dispersion as a function of temperature was almost identical from 100 to 300 K. At 400 K, however, the softening of the optical branches was more significant than that of the acoustic branches. Although the energy gap between the low-frequency and high-frequency phonons (in the range of 0.5–2.0 THz) became smaller, the energies of the optical branches were still more than double those of low-frequency acoustic branches. This indicated that the three-phonon scattering processes, by which two acoustic phonons combined into an optical phonon, or the splitting process in the β-phase AgI was also restricted by the large energy gap. The above phonon-dispersion characteristics, i.e., (1) energy bunching and the large phonon band gap and (2) the flat phonon bands in both γ- and β-phase AgI, did not forbid four-phonon scattering processes, suggesting the important role of quartic anharmonicity in the phonon dynamics and the lattice thermal conductivity of AgI. The available three-phonon and four-phonon scattering phase spaces of γ- and β-phase AgI are calculated quantitatively [64]. As the results shown in Figs. 3(a) and 3(b), the four-phonon scattering phase spaces are even almost overwhelming in both γ- and β-phase AgI. Especially, the three-phonon scattering spaces are remarkably low at the frequency range of the "phonon band gap" in a range of 0.5–2.0 THz. The low-frequency "split acoustic bands" in γ-AgI or "intertwined acoustic bands" in β-AgI contributed to the sharply increased four-phonon scattering phase space around 0.5 to 1 THz. In addition, high-frequency "flat optical bands" over 2.7 THz exist in both γ- and β-phase AgI also result in a significant four-phonon scattering phase space. To perform a rough estimation of the strength of the four-phonon interactions, we followed Feng *et al.*'s approach and calculated the strength of the four-phonon scattering by $|\Phi_4/\Phi_3|^2/\Phi_2$ [27]. Using the self IFCs of Ag atoms at 100 K, the strengths of four-phonon scattering were estimated to be ~ 5.53 and ~ 5.66 for γ- and β-phase AgI, respectively. These values are comparable to those of materials in which four-phonon scattering is dominant, e.g., CuCl (~ 6.96) and $AgCrSe_2$ (~ 4.27 at 100 K) [25,27].

Next, we further study the anharmonic lattice dynamics of γ- and β-phase AgI by directly calculating their phonon spectral functions with and without four-phonon interactions as follows [43,46,48]:

$$S_{\bar{k},s}(\omega) = \frac{2\omega_{\bar{k},s}\Gamma_{\bar{k},s}(\omega)}{\left[\omega^2 - \omega_{\bar{k},s}^2 - 2\omega_{\bar{k},s}\Delta_{\bar{k},s}(\omega)\right]^2 + 4\omega_{\bar{k},s}^2\Gamma_{\bar{k},s}^2(\omega)},$$
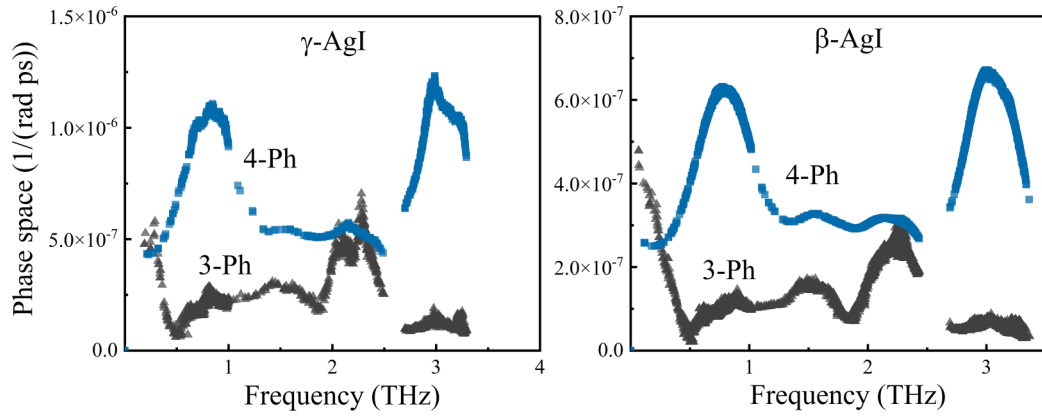
(13)

FIG. 3. Scattering phase space of (a) γ-AgI and (b) β-AgI at 300 K. Dark-gray triangles represent the phase space available for three-phonon scattering processes and blue squares represent the phase space available for four-phonon scattering processes.

where $\omega_{\vec{k},s}$ is the eigenfrequency of the phonon in the mode $\vec{k}, s$ with the wave vector $\vec{k}$ and polarization index s, and $\Gamma_{\vec{k},s}(\omega)$ and $\Delta_{\vec{k},s}(\omega)$ represent the linewidth broadening and frequency shift of the phonon self-energy $\sum_{\vec{k},s}(\omega) = \Delta_{\vec{k},s}(\omega) - i\Gamma_{\vec{k},s}(\omega)$, respectively [65]. The effect of four-phonon interactions in addition to the effect of conventional three-phonon interactions can be readily taken into consideration by simply writing the phonon self-energy $\sum_{\vec{k},s}(\omega)$ as a sum of the first-order cubic perturbation and the second-order quartic perturbation $\sum_{\vec{k},s}(\omega) = \sum'_{\vec{k},s}(\omega) + \sum''_{\vec{k},s}(\omega)$. For the expressions for the phonon self-energy see the Supplemental Material for details [25,66]. Figures 4 and 5 display the calculated $S_{\vec{k},s}(\omega)$ for γ- and β-AgI in the temperature range of 100–400 K with/without second-order quartic anharmonic perturbations, respectively. When considering only first-order cubic perturbations in γ-AgI [Figs. 4(a)–4(d)], the LA branch in the energy range of 0.8–1.5 THz was broadened with increasing temperature, which originated from the

Fermi resonance of three acoustic phonons [67]. At 400 K, the three-phonon Fermi resonance became more significant, which resulted in a significant wide and fuzzy belt [the region indicated by the dashed square in Fig. 4(d)] on the LA branch. More importantly, the spectral functions of both the TA and LA branches softened with increasing temperature, whereas the TA phonons were unable to maintain their stability at 400 K. As a consequence, the three-phonon interactions alone would lead to dynamic structural instability below the phase-transition temperature of 420 K in γ-AgI [68,69]. However, as shown in Figs. 4(e)–4(h) such dynamic structural instability was well compensated for by the second-order quartic anharmonic interactions. Furthermore, the quartic anharmonicity also led to a remarkable broadening of the TA branches. The degenerate TA phonons even split into two diffuse bands at 400 K, and the three acoustic phonon branches became parallel to each other. Meanwhile, the conservation of energy did not rule out the traditional combination- or inverse-splitting processes. The large phonon energy gap between the TA
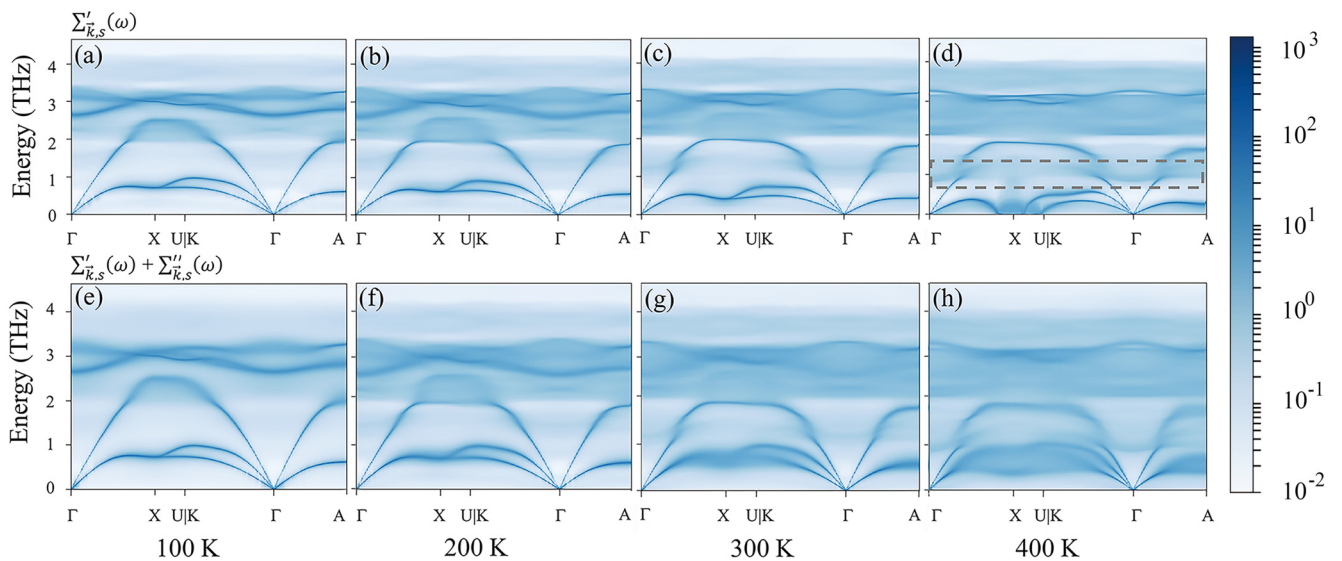

FIG. 4. Phonon spectral functions including (a)–(d) only three-phonon scattering and (e)–(h) both three-phonon and four-phonon scattering processes in the temperature range of 100–400 K for γ-phase AgI.
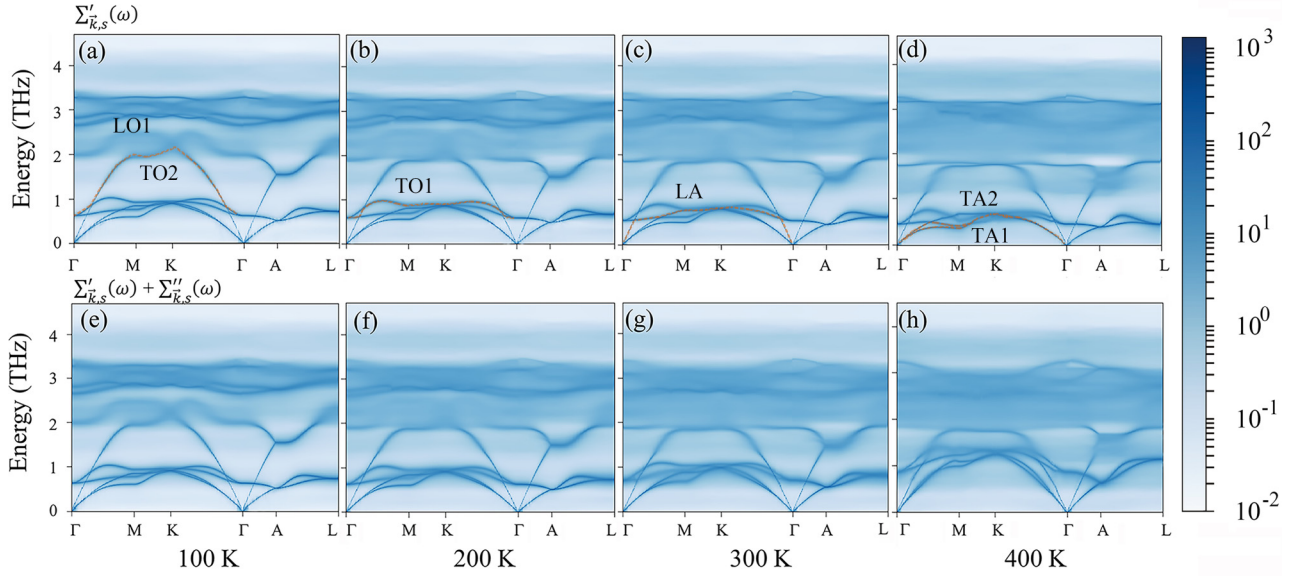
FIG. 5. Phonon spectral functions including (a)–(d) only three-phonon scattering and (e)–(h) both three-phonon and four-phonon scattering processes in the temperature range of 100–400 K for β-phase AgI.

and LA branches and the parallel acoustic branches contributed to a broad phase space for four-phonon scattering as well.

The anharmonic lattice dynamics of β-AgI are shown in Fig. 5, in which the low-frequency optical branches intertwined with the acoustic branches and formed bunching below 1 THz. According to Yang *et al.*, three-phonon processes have difficulty occurring on such acoustic branches owing to energy-conservation rules, which thus result in weak three-acoustic phonon scattering [28,70,71]. To better identify those intertwined phonon modes, the acoustic and low-energy optical phonons are highlighted in Figs. 5(a)–5(d). We surprisingly found that the low TA1/TA2/LA/TO1 frequency branches and the LO1 optical branch (in the range of 2–2.5 THz) could also combine into a high-frequency phonon, which gave rise to nearly flat optical branches and the notable broadening of these phonon bands above 2 THz. With increasing temperature, the fully diffused optical branches showed significant three-phonon scattering. The low-frequency phonons (acoustic phonons and TO1/TO2) slightly shifted to lower frequencies with increasing temperature [Figs. 5(a)–5(d)]. In contrast, they were slightly more diffuse and shifted inversely to high frequencies with $\sum_{\bar{k},s}^{''}(\omega)$, as shown in Figs. 5(e) and 5(f). The four-phonon scattering processes also played a role in β-AgI.

To further demonstrate the roles of the four-phonon interactions in the phonon-phonon scattering processes in AgI, the phonon spectral functions including both $\sum_{\bar{k},s}^{'}(\omega)$ and $\sum_{\bar{k},s}^{''}(\omega)$ (solid lines) at the U point for γ-AgI and the M point for β-AgI, along with the three-phonon interactions as a reference (dashed lines), are provided in Fig. 6. To see the frequency shifts due to the phonon renormalization more clearly, vertical bars are used to indicate the eigenfrequencies $\omega_{\bar{k},s}$ of the bare phonons. Figures 6(a)–6(d) display the temperature-dependent $S_{\bar{k},s}(\omega)$ curves at the U point of the γ-phase AgI.

Without $\sum_{\bar{k},s}^{''}(\omega)$, the $S_{\bar{k},s}(\omega)$ curves of different phonon modes, other than the LA branch, showed typical Lorentzian shapes in the temperature range of 100–400 K. The Lorentzian shape even remained near the structural phase-transition temperature, which was indicative of weak three-phonon interactions. Instead, the spectral function of the LA branch resembled a saddle at 200 K, and it downshifted to a low-frequency region with increasing temperature. Such a special double-peak structure was also found in the CuCl system due to Fermi resonance [25,43,67]. With both the three-phonon interactions $\sum_{\bar{k},s}^{'}(\omega)$ and four-phonon interactions $\sum_{\bar{k},s}^{''}(\omega)$, the most important feature of the phonon's spectral function is that the peaks of TA1 and TA2 became weaker and broader, which indicated significant renormalization of TA phonons. Around T_c, the line shape of the TA1 branch resembled a saddle, while the TA2 showed an inclined slide type. They are both far from the typical Lorentzian shape. In this case, strong anharmonic four-phonon Fermi resonance occurred and the phonon quasiparticle description broke down. In addition, the optical branches became weaker and broader as well when the high-order four-phonon interactions were considered. For β-AgI, the temperature-dependent $S_{\bar{k},s}(\omega)$ at the M point is shown in Figs. 6(e)–6(h). The line shapes of the acoustic branches also became weaker and broader with $\sum_{\bar{k},s}^{''}(\omega)$. The peak positions of the dressed phonons coincided with their eigenfrequencies $\omega_{\bar{k},s}$ after the inclusion of $\sum_{\bar{k},s}^{''}(\omega)$, which revealed that the frequency shift caused by the lowest-order perturbation was well compensated for. Unlike γ-AgI, the spectral functions of β-AgI exhibited well-defined Lorentzian broadening of individual peaks [43]. Nevertheless, $\sum_{\bar{k},s}^{''}(\omega)$ affected all the acoustic branches and also lowered κ_l. Thus, the overestimation of the κ_l of AgI in previous theoretical work was likely caused by neglecting four-phonon interactions [39,40]. Similar results for γ- and β-phase AgI can also
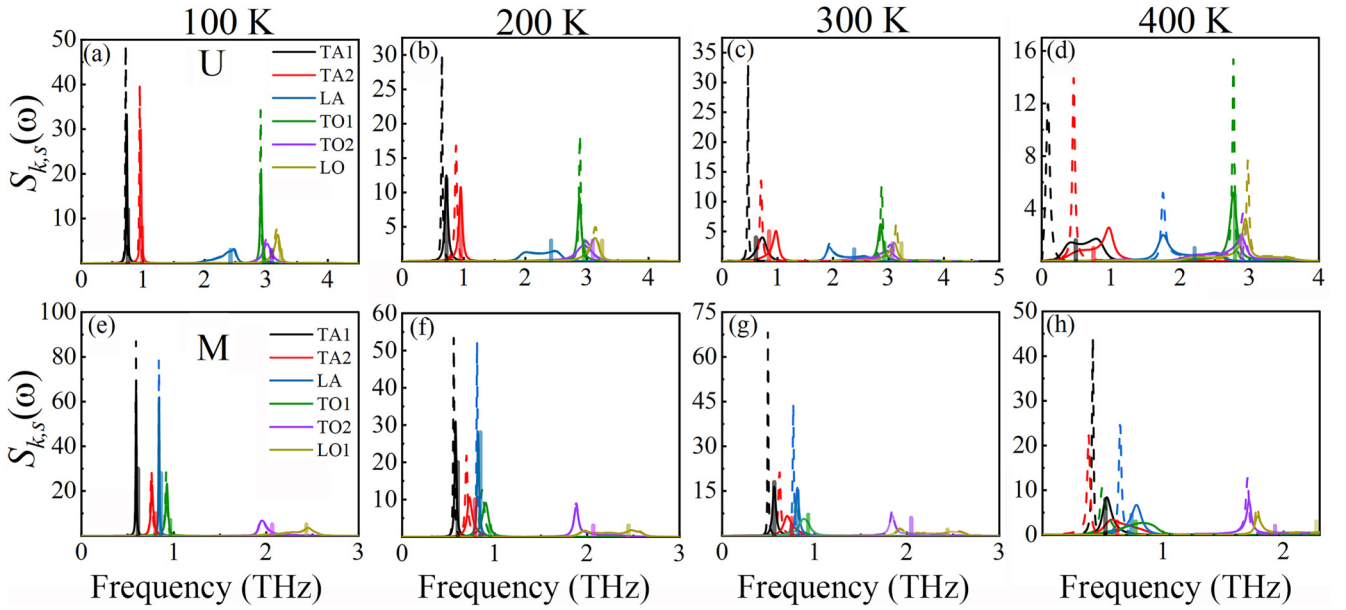
FIG. 6. Spectral functions $S_{k,s}(\omega)$ at the (a)–(d) U point for γ-AgI and (e)–(h) M point for β-AgI. Dashed lines are the results calculated with the three-phonon interactions $\sum'_{\vec{k},s}(\omega)$ alone, while the solid lines are the results calculated with both three- and four-phonon interactions $\sum'_{\vec{k},s}(\omega) + \sum''_{\vec{k},s}(\omega)$. Colored vertical bars denote the phonon eigenfrequency $\omega_{\vec{k},s}$. Linewidth broadening and frequency shift due to the four-phonon interactions are evident.

be found at other representative reciprocal points (see Fig. S3 for further details in Supplemental Material).

As a crude estimation of whether the high-order quartic anharmonicity played a critical role in the ultralow lattice thermal conductivity in AgI, we also calculated the linewidths of acoustic phonons. Figure 7 displays the imaginary parts $\Gamma_{\vec{k},s}(\omega)$ for γ- and β-phase AgI at different temperatures. As the linewidth of γ-phase AgI increased with temperature, the difference between $\Gamma''_{\vec{k},s}(\omega)$ and $\Gamma'_{\vec{k},s}(\omega)$ became significant,

especially for TA branches. For example, with increasing temperature, the linewidth with both three-phonon and four-phonon interactions ($\Gamma' + \Gamma''$) of the TA1 (TA2) branch at the U point for γ-phase AgI increased substantially from 0.010 (0.010) THz at 100 K to 0.259 (0.249) THz at 400 K, while the linewidth of the TA1 (TA2) branch with Γ' alone was only 0.007 (0.008) THz at 100 K and increased marginally to 0.014 (0.039) THz at 400 K. For β-phase AgI, the $\Gamma' + \Gamma''$ of the TA1 (TA2) branch at the M point increased from 0.004
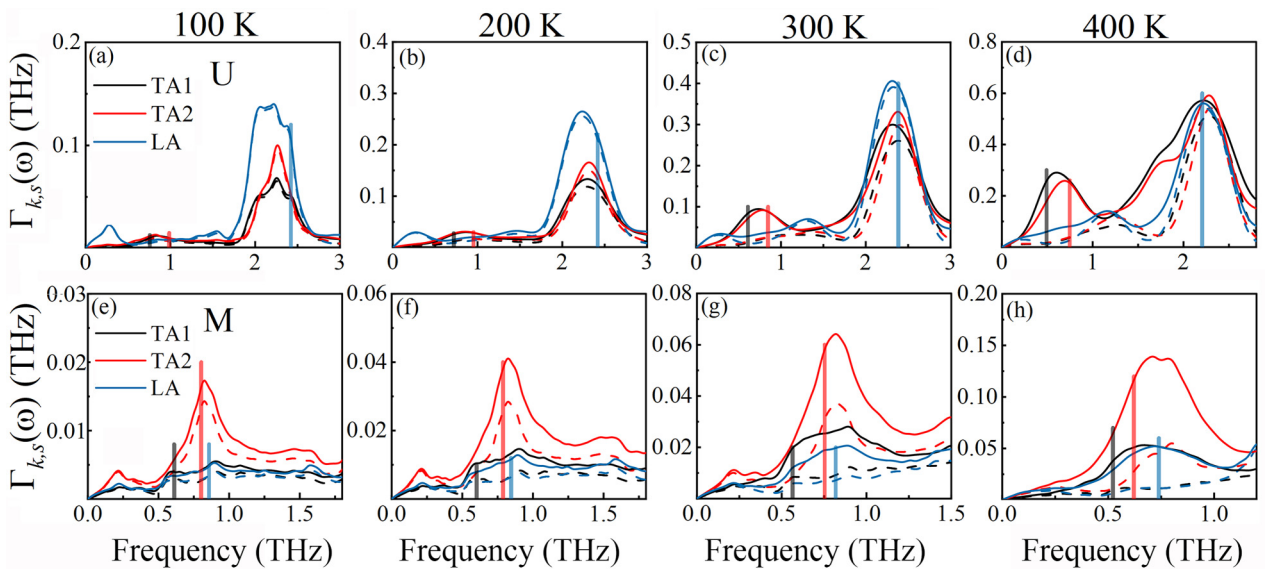

FIG. 7. Imaginary part $\Gamma'_{\vec{k},s}(\omega)$ (with three-phonon interactions shown by dashed lines) and $\Gamma''_{\vec{k},s}(\omega)$ (with three- and four-phonon interactions shown by solid lines) of the acoustic phonon self-energy functions for the (a)–(d) γ phase at the zone-boundary point U and the (e)–(h) β phase at the point M at different temperatures.
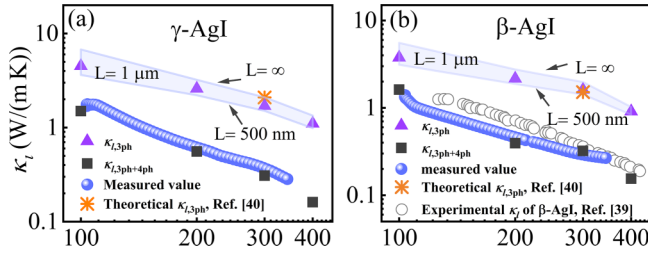
FIG. 8. Experimental and theoretical thermal conductivities of (a) the γ phase and (b) β phase as functions of temperature. Blue spheres represent our measured thermal conductivity values. Measured κ_l values in (b) are comparable to the literature values [39] (gray empty circles). Considering the boundary size, the theoretical $\kappa_{l,3ph}$ with a boundary size range from 500 nm to ∞ is shown in the purple-shaded area, along with the $\kappa_{l,3ph}$ of 1 μm inside (purple triangles). The theoretical $\kappa_{l,3ph}$ of γ- and β-AgI was in good agreement with the previous theoretical work (orange asterisks) in Ref. [40]. The calculated $\kappa_{l,3ph+4ph}$ (black squares) were consistent with our measured thermal conductivities.

(0.018) THz at 100 K to 0.039 (0.117) THz at 400 K, while the Γ' of the TA1 (TA2) branch increased from 0.003 (0.014) THz at 100 K to 0.01 (0.028) THz at 400 K. It is interesting that the peaks of $\Gamma'_{\vec{k},s}(\omega)$ and $\Gamma'_{\vec{k},s}(\omega) + \Gamma''_{\vec{k},s}(\omega)$ almost coincided with the bare phonon frequency of the LA branch, which was indicative of a combined three-phonon and four-phonon resonance in β-AgI. We also employed $\tau_{4ph}^{-1}/\tau_{3ph}^{-1}$ to compare the scattering rates for these two individual processes, where τ_{4ph}^{-1} and τ_{3ph}^{-1} represent the four-phonon scattering rate and the three-phonon scattering rate, respectively [66]. According to our calculations, the exceptionally large four-phonon scattering of the TA phonons in the γ-phase AgI at the U point resulted in $\tau_{4ph}^{-1}/\tau_{3ph}^{-1} \sim 14.60$ (5.58), 6.42 (3.42), 2.26 (1.71), and 1.43 (1.25) for the TA1 (TA2) branch at 400, 300, 200, and 100 K, respectively. It is clear that TA phonons were overwhelmed exclusively by resonating four-phonon scattering. In comparison, the $\tau_{4ph}^{-1}/\tau_{3ph}^{-1}$ ratios of the β phase were 2.80 (3.18), 2.46 (1.87), 1.70 (1.46), and 1.33(1.28) for the TA1 (TA2) branch at 400, 300, 200, and 100 K, respectively. As a result, stronger quartic anharmonicity arose in the γ-phase AgI due to the flat bands, which allowed both the traditional phonon absorption and emission processes and four-phonon Fermi resonance.

C. Lattice thermal conductivity

In this section, we compare the theoretical lattice thermal conductivities when including both three-phonon and four-phonon processes for γ- and β-phase AgI with the experimental results (Fig. 8). The theoretical results including only three-phonon interactions, as calculated by Togo, are also provided as a comparison [40]. The variable-temperature XRD results in Fig. S2 verified that our single-phase β-AgI crystal was successfully synthesized, and there was no transition between the β- and γ-phase AgI in the temperature range of 300–400 K. Note that for γ-AgI, we had to deduce its κ_l from the measured κ_l of single-phase β-AgI and their mixtures because we were unable to synthesize single-phase γ-AgI. According to the method proposed by Maxwell [72],

the thermal conductivity of the mixture can be obtained as follows:

$$\kappa_m = \frac{\kappa_A[\kappa_B + 2\kappa_A - 2P_B(\kappa_A - \kappa_B)]}{\kappa_B + 2\kappa_A + P_B(\kappa_A - \kappa_B)} \quad (14)$$

where κ_A and κ_B represent the thermal conductivities of single-phase A and B, respectively, P_B is the phase-volume fraction of phase B, and κ_m is the thermal conductivity of the two-phase mixture. The measured κ_l values of the multiphase AgI mixture are displayed in Fig. 8(a). The measured κ_l values for the β-phase AgI ($\kappa_l \sim 0.29$ W/m K at 300 K) were consistent with the reported results [Fig. 8(b)]. The deduced κ_l of γ-AgI was only 0.36 W/m K at 300 K and was much smaller than the value predicted (~ 2.09 W/m K) [40] in previous theoretical work, in which only three-phonon interactions were considered. Using a similar theoretical approach, we first compared the lattice thermal conductivities of γ- and β-phase AgI calculated solely with three-phonon scattering ($\kappa_{l,3ph}$) and those calculated with both three-phonon/four-phonon scattering ($\kappa_{l,3ph+4ph}$). As shown in Fig. 8, the theoretical $\kappa_{l,3ph}$ of γ-AgI with a boundary size of ∞ was ~ 2.10 W/m K, which was consistent with the theoretical result of 2.09 W/m K at 300 K [40]. In the meantime, the $\kappa_{l,3ph}$ of β-AgI with an intermediate boundary size of 1 μm was ~ 1.62 W/m K at 300 K, which was comparable to the predicted value of ~ 1.51 W/m K in previous work [40]. In the proximity of the phase-transition temperature, the calculated $\kappa_{l,3ph}$ of both the γ- and β-phase AgI (at 400 K) decreased and deviated from the general $\kappa_l \sim T^{-1}$ rule for materials with dominant three-phonon scattering [27], suggesting the emergence of even stronger anharmonicity. However, when we considered the four-phonon scattering process, the theoretical $\kappa_{l,3ph+4ph}$ in the γ-phase AgI decreased noticeably from ~ 1.69 to 0.32 W/m K at 300 K, which agreed with the measured value (0.36 W/m K). The mean value of the theoretical $\kappa_{l,3ph+4ph}$ for β-phase AgI decreased from 1.62 to 0.32 W/m K, which was comparable to the experimental value (~ 0.29 W/m K) as well.

IV. DISCUSSION AND CONCLUSIONS

In AgI, the rattling of Ag ions, the dispersionless phonon band structure, and phonon Fermi resonance are intimately related to each other and are the main cause of the ultralow κ_l. This correlation is not solely restricted to AgI but can also be readily applied to other material systems. The key factor here is the low-frequency flat phonon dispersion. First, as we have pointed out in Sec. III A, the general formulation given by Eq. (12) implies that a large MSD can be achieved by a low atomic mass as well as dense low-frequency phonon vibrations. Therefore, materials with characteristic flat phonon dispersion at low frequencies naturally lead to large $(1 + 2n_\nu)\omega_\nu^{-1}|e_\nu^\alpha(j, q)|^2$ and they are potential candidates having large MSDs (or MSD differences) [45]. However, the dispersionless phonon branch can be viewed as localized vibrations of atoms within a potential well, of which the depth is approximately proportional to ω_ν^2 [73]. In fact, the so-called "localized vibration atoms" can never completely localize, only weak coupling with the surroundings. In the case of the low-frequency limit ($\omega_\nu \rightarrow 0$,

or ω_v is much smaller than the Debye frequency), the atoms are subjected to a shallow potential or weak interactions in at least one direction, thus resulting in large-amplitude atom vibrations or MSDs. Second, the low-frequency flat phonon dispersion substantially lowered the phonon group velocities, usually from the order of 10^3 to 10^2 m/s. This localized nature, along with the dense DOS of the dispersionless phonons, would significantly reduce the corresponding heat conduction by these phonons. In addition, the low-frequency dispersionless mode might also suppress the dispersive acoustic phonons and reduce their velocities. In the simplest condition, the acoustic phonon velocity v is determined by the frequency of the dispersionless phonon at the zone boundary ω_s and the zone-boundary reciprocal point with $v = \omega_s/k$. As a result, the lower the vibrational frequency ω_s of the rattling atoms is, the smaller the sound speed v and κ_l become. Finally, the flat phonon dispersion could also increase both the three-phonon and four-phonon scattering phase space substantially, thus reducing the phonon relaxation time and κ_l. Using the flat phonon dispersion as a fingerprint and guide for materials with low κ_l values, we can summarize some of the rattling systems with characteristic flat phonon dispersion. The first class includes materials that have cagelike structures with atoms rattling in the center, which are weakly bounded in three dimensions and tend to form dispersionless phonon band structures with three flat phonon bands, i.e., SbNaLi$_2$ [24], CsPbBr$_3$ [61], KCaF$_3$ [74], and YbFe$_4$Sb$_{12}$ [75]. The second class includes materials with quasi–two-dimensional structures like AgCrSe$_2$ [25] and Mg$_3$Bi$_2$ [76], which form two flat phonon bands due to the weak in-plane bonding. The last group includes materials with chainlike rattling structures, i.e., TlInTe$_2$ [62] and InTe [77], in which a single low-frequency dispersionless phonon band structure is formed as a result of the weak bonds along the chain. In addition to the rattling systems, some layered thermoelectric materials with significantly decreased κ_l values also exhibit characteristic flat phonon dispersion, such as single-layer MoTe$_2$ [78], PbSe, and GeSe [79]. However, the four-phonon scattering or higher-order interactions in those single-layer structures with

dispersionless phonon bands have rarely been discussed. Our work has implications for materials with flat phonon band structures and the study of these materials is within the scope of our future work.

In summary, the temperature-dependent thermal transport properties of γ- and β-AgI were studied by many-body perturbation theory and phonon Boltzmann transport theory in this work. The large difference in the MSDs between Ag$^+$ and I$^-$ is identified as the reason for the characteristic rattling feature and inherent low-frequency, nearly flat local phonon vibrations, which give rise to strong anharmonicity and resonant four-phonon scattering. Considering fourth-order anharmonicity, the broadened spectrum of the flat TA branches in the γ-AgI was indicative of the overwhelming role of four-phonon Fermi resonant scattering processes. The "flat-band" effect also appeared in β-AgI due to the presence of diffuse and broad nearly flat optical branches, namely, the three- and four-phonon resonances were equally important. The theoretical values of both γ-phase and β-phase AgI were in good agreement with the experiments in the temperature range of 100–400 K. Furthermore, the weak-bonding rattling mode, dispersionless phonon band structure, and phonon resonance were suggested to be intimately related to each other, which resulted in the low κ_l of AgI. Such a relationship is not restricted to AgI, but also provides insights for finding materials with ultralow lattice thermal conductivities.

[1] B. Poudel, Q. Hao, Y. Ma, Y. Lan, A. Minnich, B. Yu, X. Yan, D. Wang, A. Muto, D. Vashaee, X. Chen, J. Liu, M. S. Dresselhaus, G. Chen, and Z. Ren, High-thermoelectric performance of nanostructured bismuth antimony telluride bulk alloys, Science **320**, 634 (2008).

[2] W. Li, N. Mingo, L. Lindsay, D. A. Broido, D. A. Stewart, and N. A. Katcho, Thermal conductivity of diamond nanowires from first principles, Phys. Rev. B **85**, 195436 (2012).

[3] K. Biswas, J. He, I. D. Blum, C.-I. Wu, T. P. Hogan, D. N. Seidman, V. P. Dravid, and M. G. Kanatzidis, High-performance bulk thermoelectrics with all-scale hierarchical architectures, Nature (London) **489**, 414 (2012).

[4] M. J. Lee, J. H. Ahn, J. H. Sung, H. Heo, S. G. Jeon, W. Lee, J. Y. Song, K. H. Hong, B. Choi, S. H. Lee, and M. H. Jo, Thermoelectric materials by using two-dimensional materials with negative correlation between electrical and thermal conductivity, Nat. Commun. **7**, 12011 (2016).

[5] D. J. Voneshen, K. Refson, E. Borissenko, M. Krisch, A. Bosak, A. Piovano, E. Cemal, M. Enderle, M. J. Gutmann, M. Hoesch, M. Roger, L. Gannon, A. T. Boothroyd, S. Uthayakumar, D. G. Porter, and J. P. Goff, Suppression of thermal conductivity by rattling modes in thermoelectric sodium cobaltate, Nat. Mater. **12**, 1028 (2013).

[6] W. Li and N. Mingo, Thermal conductivity of fully filled skutterudites: Role of the filler, Phys. Rev. B **89**, 184304 (2014).

[7] J. He and T. M. Tritt, Advances in thermoelectric materials research: Looking back and moving forward, Science **357**, eaak9997 (2017).

[8] J. Li, W. Hu, and J. Yang, High-throughput screening of rattling-induced ultralow lattice thermal conductivity in semiconductors, J. Am. Chem. Soc. **144**, 4448 (2022).

[9] J. L. Cohn, G. S. Nolas, V. Fessatidis, T. H. Metcalf, and G. A. Slack, Glasslike Heat Conduction in High-Mobility Crystalline Semiconductors, Phys. Rev. Lett. **82**, 779 (1999).

[10] B. C. Sales, D. Mandrus, and R. K. Williams, Filled skutterudite antimonides: A new class of thermoelectric materials, Science **272**, 1325 (1996).

[11] S. Mukhopadhyay, D. S. Parker, B. C. Sales, A. A. Puretzky, M. A. McGuire, and L. Lindsay, Two-channel model for ultralow thermal conductivity of crystalline Tl_3VSe_4, Science **360**, 1455 (2018).

[12] T. M. Brenner, C. Gehrmann, R. Korobko, T. Livneh, D. A. Egger, and O. Yaffe, Anharmonic Host Lattice Dynamics Enable Fast Ion Conduction in Superionic AgI, Phys. Rev. Mater. **4**, 115402 (2020).

[13] H. Liu, X. Shi, F. Xu, L. Zhang, W. Zhang, L. Chen, Q. Li, C. Uher, T. Day, and G. J. Snyder, Copper ion liquid-like thermoelectrics, Nat. Mater. **11**, 422 (2012).

[14] F. Damay, S. Petit, S. Rols, M. Braendlein, R. Daou, E. Elkaïm, F. Fauth, F. Gascoin, C. Martin, and A. Maignan, Localised Ag^+ vibrations atthe origin of ultralow thermal conductivity in layered thermoelectric $AgCrSe_2$, Sci. Rep. **6**, 23415 (2016).

[15] Z. Deng, Z. Zhu, I. H. Chu, and S. P. Ong, Data-driven first-principles methods for the study and design of alkali superionic conductors, Chem. Mater. **29**, 281 (2017).

[16] D. A. Broido, A. Ward, and N. Mingo, Lattice thermal conductivity of silicon from empirical interatomic potentials, Phys. Rev. B **72**, 014308 (2005).

[17] D. A. Broido, M. Malorny, G. Birner, N. Mingo, and D. A. Stewart, Intrinsic Lattice Thermal Conductivity of Semiconductors from First Principles, Appl. Phys. Lett. **91**, 231922 (2007).

[18] L. Lindsay, C. Hua, X. L. Ruan, and S. Lee, Survey of ab initio phonon thermal transport, Mater. Today Phys. **7**, 106 (2018).

[19] N. Mingo, Calculation of Si nanowire thermal conductivity using complete phonon dispersion relations, Phys. Rev. B **68**, 113308 (2003).

[20] A. J. H. Mcgaughey, A. Jain, H.-Y. Kim, and B. Fu, Phonon properties and thermal conductivity from first principles, lattice dynamics, and the Boltzmann transport equation, J. Appl. Phys. **125**, 011101 (2019).

[21] T. Feng and X. Ruan, Quantum mechanical prediction of four-phonon scattering rates and reduced thermal conductivity of solids, Phys. Rev. B **93**, 045202 (2016).

[22] S. Mukhopadhyay, D. Bansal, O. Delaire, D. Perrodin, E. Bourret-Courchesne, David J. Singh, and L. Lindsay, The curious case of cuprous chloride: Giant thermal resistance and anharmonic quasiparticle spectra driven by dispersion nesting, Phys. Rev. B **96**, 100301(R) (2017).

[23] Z. Zhang, Y. Guo, M. Bescond, J. Chen, M. Nomura, and S. Volz, Heat Conduction Theory Including Phonon Coherence, Phys. Rev. Lett. **128**, 015901 (2022).

[24] A. Jain, Single-channel or multichannel thermal transport: Effect of higher-order anharmonic corrections on the predicted phonon thermal transport properties of semiconductors, Phys. Rev. B **106**, 045207 (2022).

[25] L. Xie, J. H. Feng, R. Li, and J. Q. He, First-Principles Study of Anharmonic Lattice Dynamics in Low Thermal Conductivity $AgCrSe_2$: Evidence for a Large Resonant Four-Phonon Scattering, Phys. Rev. Lett. **125**, 245901 (2020).

[26] See Supplemental Material at http://link.aps.org/supplemental/10.1103/PhysRevB.107.064308 for detailed information regarding the schematic of phonon-phonon scattering processes, mean-squared displacements based on the harmonic approximation, rietveld refinement of x-ray diffraction, and the spectral

functions (and imaginary part of phonon self-energy functions) at other representative reciprocal points.

[27] T. Feng, L. Lindsay, and X. Ruan, Four-phonon scattering significantly reduces intrinsic thermal conductivity of solids, Phys. Rev. B **96**, 161201(R) (2017).

[28] X. Yang, T. Feng, and J. Li, and X. Ruan, Stronger role of four-phonon scattering than three-phonon scattering in thermal conductivity of III-V semiconductors at room temperature, Phys. Rev. B **100**, 245203 (2019).

[29] J. Tallon, Molecular-Dynamics Simulation of the Phase Behavior of AgI, Phys. Rev. Lett. **57**, 2427 (1986).

[30] G. Burley, Kinetics and mechanism of the low-cubic to hexagonal phase transformation of silver iodide, J. Phys. Chem. **68**, 1111 (1964).

[31] G. Burley, The "memory effect" in silver iodide, Acta Crystallogr. **23**, 1 (1967).

[32] A. Aznar, P. Lloveras, M. Romanini, M. Barrio, J.-L. Tamarit, C. Cazorla, D. Errandonea, N. D. Mathur, A. Planes, X. Moya, and L. Mañosa, Giant barocaloric effects over a wide temperature range in superionic conductor AgI, Nat. Commun. **8**, 1851 (2017).

[33] R. Shaviv, E. F. W. Jr, F. Grønvold, S. Stølen, A. Inaba, H. Fujii, and C. Hideaki, Heat capacity, thermodynamic properties, and transitions of silver iodide, J. Chem. Thermodyn. **21**, 631 (1989).

[34] M. Cardona, Optical properties of the silver and cuprous halides, Phys. Rev. **129**, 69 (1963).

[35] R. B. Wilsey, LIII. The crystalline structures of silver iodide, Philos. Mag. **46**, 273 (1923).

[36] D. R. Mills, C. M. Perrott, and N. H. Fletcher, The production of single crystals of AgI, J. Cryst. Growth **6**, 266 (1970).

[37] W. Bührer, R. M. Nicklow, and P. Briiesch, Lattice dynamics of β- (silver iodide) by neutron scattering, Phys. Rev. B **17**, 3362 (1978).

[38] X. M. Zhang, R. S. Ma, X. C. Liu, E. K. Liu, G. D. Liu, Z. Y. Liu, W. H. Wang, and G. H. Wu, Topological insulators in hexagonal wurtzite-type binary compounds, Mater. Sci. **103**, 57012 (2013).

[39] M. C. Goetz and J. A. Cowen, The thermal conductivity of silver iodide, Solid State Commun. **41**, 293 (1982).

[40] A. Togo, L. Chaput, and I. Tanaka, Distributions of phonon lifetimes in Brillouin zones, Phys. Rev. B **91**, 094306 (2015).

[41] G. Kresse and J. Furthmüller, Efficient iterative schemes for ab initio total-energy calculations using a plane-wave basis set, Phys. Rev. B **54**, 11169 (1996).

[42] G. Kresse and J. Furthmüller, Efficiency of ab-initio total energy calculations for metals and semiconductors using a plane-wave basis set, Comput. Mater. Sci. **6**, 15 (1996).

[43] N. Shulumba, O. Hellman, and A. J. Minnich, Intrinsic localized mode and low thermal conductivity of PbSe, Phys. Rev. B **95**, 014302 (2017).

[44] O. Hellman and I. A. Abrikosov, Temperature-dependent effective third-order interatomic force constants from first principles, Phys. Rev. B **88**, 144301 (2013).

[45] A. Togo and I. Tanaka, First principles phonon calculations in materials science, Scr. Mater. **108**, 1 (2015).

[46] B. S. Semwal and P. K. Sharma, Thermal conductivity of an anharmonic crystal, Phys. Rev. B **5**, 3909 (1972).

[47] R. Peierls, Zur kinetischen Theorie der Wärmeleitung in Kristallen, Ann. Phys. **395**, 1055 (1929).

[48] A. A. Maradudin and A. E. Fein, Scattering of neutrons by an anharmonic crystal, Phys. Rev. **128**, 2589 (1962).

[49] B. H. Toby, EXPGUI, a graphical user interface for GSAS, J. Appl. Crystallogr. **34**, 210 (2001).

[50] B. H. Toby and R. B. V. Dreele, GSAS-II: The genesis of a modern open-source all purpose crystallography software package, J. Appl. Crystallogr. **46**, 544 (2013).

[51] O. Maldonado, Pulse method for simultaneous measurement of electric thermopower and heat conductivity at low temperatures, Cryogenics **32**, 908 (1992).

[52] A. B. Gordienko, N. G. Kravchenko, and A. N. Sedelnikov, Physics of semiconductors and dielectrics ab initio calculations of the lattice dynamics of silver halides, Russ. Phys. J. **53**, 692 (2010).

[53] A. Yoshiasa, A. Inaba, T. Ishii, and K. Koto, A phase transition of AgI at 150 K, Solid State Ionics **79**, 67 (1995).

[54] R. C. Shukla and E. R. Cowley, Helmholtz free energy of an anharmonic crystal to $O(\lambda^4)$, Phys. Rev. B **3**, 4055 (1971).

[55] O. Hellman, P. Steneteg, I. A. Abrikosov, and S. I. Simak, Temperature dependent effective potential method for accurate free energy calculations of solids, Phys. Rev. B **87**, 104111 (2013).

[56] A. Yoshiasa and H. Maed, Anharmonic effective pair potentials of β- and α-AgI determined by I K-edge EXAFS, Solid State Ionics **121**, 175 (1999).

[57] A. Yoshiasa, K. Koto, H. Maeda, and T. Ishii, The mean-square relative displacement and displacement correlation functions in tetrahedrally and octahedrally coordinated $A^N B^{8-N}$ crystals, Jpn. J. Appl. Phys. **36**, 781 (1997).

[58] A. Jain, Multichannel thermal transport in crystalline Tl_3VSe_4, Phys. Rev. B **102**, 201201(R) (2020).

[59] Y. Xia, K. Pal, J. He, V. Ozoliņš, and C. Wolverton, Particlelike Phonon Propagation Dominates Ultralow Lattice Thermal Conductivity in Crystalline Tl_3VSe_4, Phys. Rev. Lett. **124**, 065901 (2020).

[60] W. Qiu, L. Wu, X. Ke, J. Yang, and W. Zhang, Diverse lattice dynamics in ternary Cu-Sb-Se compounds, Sci. Rep. **5**, 13643 (2015).

[61] J. Lahnsteiner and M. Bokdam, Anharmonic lattice dynamics in large thermodynamic ensembles with machine-learning force fields: $CsPbBr_3$, a phonon liquid with Cs rattlers, Phys. Rev. B **105**, 024302 (2022).

[62] M. K. Jana, K. Pal, A. Warankar, P. Mandal, U. V. Waghmare, and K. Biswas, Intrinsic rattler-induced low thermal conductivity in Zintl type $TlInTe_2$, J. Am. Chem. Soc. **139**, 4350 (2017).

[63] L. Lindsay, D. A. Broido, and T. L. Reinecke1, First-Principles Determination of Ultrahigh Thermal Conductivity of Boron Arsenide: A Competitor for Diamond? Phys. Rev. Lett. **111**, 025901 (2013).

[64] Z. Han, X. Yang, W. Li, T. Feng, and X. Ruan, Four-Phonon: An extension module to ShengBTE for computing four-phonon scattering rates and thermal conductivity, Comput. Phys. Commun. **270**, 108179 (2022).

[65] K. N. Pathak, Theory of anharmonic crystals, Phys. Rev. **139**, A1569 (1965).

[66] D. J. Ecsedy and P. G. Klernens, Thermal resistivity of die ectric crystals due to four-phonon processes and optical modes, Phys. Rev. B **15**, 5957 (1977).

[67] G. Kanellis, W. Kress, and H. Bilz, Fermi Resonance in the Phonon Spectra of Copper Halides, Phys. Rev. Lett. **56**, 938 (1986).

[68] Đ. Dangić, O. Hellman, S. Fahy, and I. Savić, The origin of the lattice thermal conductivity enhancement at the ferroelectric phase transition in GeTe, npj Comput. Mater. **7**, 57 (2021).

[69] U. D. Wdowik, K. Parlinski, S. Rols, and T. Chatterji, Soft-phonon mediated structural phase transition in GeTe, Phys. Rev. B **89**, 224306 (2014).

[70] N. K. Ravichandran and D. Broido, Exposing the hidden influence of selection rules on phonon–phonon scattering by pressure and temperature tuning, Nat. Commun. **12**, 3473 (2021).

[71] R. Yang, S. Yue, Y. Quan, and B. Liao, Crystal symmetry based selection rules for anharmonic phonon-phonon scattering from a group theory formalism, Phys. Rev. B **103**, 184302 (2021).

[72] S. C. Cheng and R. I. Vachon, The prediction of the thermal conductivity of two and three phase solid heterogeneous mixtures, Int. J. Heat Mass Transfer **12**, 249 (1969).

[73] M. N. Luckyanova, J. Mendoza, H. Lu, B. Song, S. Huang, J. Zhou, M. Li, Y. Dong, H. Zhou, J. Garlow, L. Wu, B. J. Kirby, A. J. Grutter, A. A. Puretzky, Y. Zhu, M. S. Dresselhaus, A. Gossard, and G. Chen, Phonon localization in heat conduction, Sci. Adv. **4**, aat9460 (2018).

[74] F. Knoop, T. A. R. Purcell, M. Scheffler, and C. Carbogno, Anharmonicity measure for materials, Phys. Rev. Mater. **4**, 083809 (2020).

[75] W. Li and N. Mingo, Ultralow lattice thermal conductivity of the fully filled skutterudite $YbFe_4Sb_{12}$ due to the flat avoided-crossing filler modes, Phys. Rev. B **91**, 144304 (2015).

[76] J. Ding, T. L. Atkins, M. Calderón-Cueva, A. Banerjee, D. L. Abernathy, A. Said, A. Zevalkink, and O. Delaire, Soft anharmonic phonons and ultralow thermal conductivity in $Mg_3(Sb, Bi)_2$ thermoelectrics, Sci. Adv. **7**, abg1449 (2021).

[77] M. K. Jana, K. Pal, U. V. Waghmare, and K. Biswas, The origin of ultralow thermal conductivity in InTe: Lone-pair-induced anharmonic rattling, Angew. Chem. Int. Ed. Engl. **55**, 7792 (2016).

[78] X.-J. Yan, Y.-Y. Lv, L. Li, X. Li, S.-H. Yao, Y.-B. Chen, X.-P. Liu, H. Lu, M.-H. Lu, and Y.-F. Chen, Investigation on the phase-transition-induced hysteresis in the thermal transport along the c-axis of $MoTe_2$, npj Quant. Mater. **2**, 31 (2017).

[79] P. F. Liu, T. Bo, J. Xu, W. Yin, J. Zhang, F. Wang, O. Eriksson, and B. T. Wang, First-principles calculations of the ultralow thermal conductivity in two-dimensional group-IV selenides, Phys. Rev. B **98**, 235426 (2018).